





Monolithic chalcogenide glass waveguide integrated interband cascaded laser

HONGTAO LIN,¹  CHUL SOO KIM,² LAN LI,¹  MIJIN KIM,³ WILLIAM W. BEWLEY,² CHARLES D. MERRITT,² CHADWICK L. CANEDY,² IGOR VURGAFTMAN,² ANU AGARWAL,⁴ KATHLEEN RICHARDSON,⁵ JUEJUN HU,^{1,6} AND JERRY R. MEYER^{2,7}

¹Department of Materials Science and Engineering, University of Delaware, Newark, DE 19716, USA

²Code 5613, Naval Research Laboratory, Washington, DC 20375, USA

³Jacobs Corporation, Hanover, MD 21076, USA

⁴Materials Research Laboratory, Massachusetts Institute of Technology, Cambridge, MA 02139, USA

⁵The College of Optics & Photonics, Department of Materials Science and Engineering, University of Central Florida, Orlando, FL 32816, USA

⁶hujuejun@udel.edu

⁷jerry.meyer@nrl.navy.mil

Abstract: Mid-infrared photonic integrated circuits (PICs) that combine on-chip light sources with other optical components constitute a key enabler for applications such as chemical sensing, light detection, ranging, and free-space communications. In this paper, we report the monolithic integration of interband cascade lasers emitting at 3.24 μm with passive, high-index-contrast waveguides made of chalcogenide glasses. Output from the chalcogenide waveguides exhibits pulsed peak power up to 150 mW (without roll-over), threshold current density 280 A/cm², and slope efficiency 100 mW/A at 300 K, with a lower bound of 38% efficiency for coupling between the two waveguides. These results represent an important step toward the realization of fully integrated mid-infrared PICs.

© 2021 Optical Society of America under the terms of the [OSA Open Access Publishing Agreement](#)

Mid-infrared (mid-IR) photonic integration [1–6] promises chip-scale modules with significant Size, Weight, Power and Cost (SWaP-C) advantages compared to conventional systems based on bulk optics. Mid-IR photonic integrated circuits (PICs) will facilitate applications such as chemical sensing, optical spectroscopy, light detection and ranging, IR countermeasures, and free-space communications [7–11]. Significant progress has been made toward the integration of various components such as waveguides [12], resonant cavities [13], photodetectors [14], and modulators [15,16].

However, the on-chip integration of mid-IR sources continues to pose significant technical challenges. In particular, PICs on a silicon platform require heterogeneous integration with a gain medium to circumvent the intrinsic indirect bandgap of the host material. While nonlinear frequency conversion based on supercontinuum [17], frequency comb [11], or Raman soliton [18] generation may be employed, these require an external (often off-chip) pump laser. Alternative strategies include the heteroepitaxial growth of GeSn [19,20] or III-V [21] quantum wells on silicon, or bonding a III-V gain medium to Si waveguides [22,23]. The integration of a III-V epitaxial platform offers direct access to mid-IR sources such as quantum cascade lasers (QCLs) [24,25] and interband cascade lasers (ICLs) [26–29], which are now relatively mature and provide high performance. PICs can also be fabricated on the native III-V chip [6,8], and narrow-ridge QCLs (ICLs) have been monolithically integrated on the same chip with quantum (interband) cascade detectors processed from the same wafer material as the laser [30,31]. Additional techniques such as selective area regrowth and ion implantation can locally increase the bandgap to create transparent passive waveguides for integration with the lasers [32]. Low-loss passive

waveguides can also be formed by removing the absorbing active gain layers [6,33]. Finally, the hybrid integration of QCLs has been implemented by butt-coupling to waveguides fabricated on a separate chip [34].

In this work, we demonstrate an alternative route to integration in the mid-IR, namely by monolithically fabricating chalcogenide glass (ChG) waveguides on the same chip with the III-V lasers (ICLs in this case). The active and passive waveguides are then connected by butt coupling, as shown schematically in Fig. 1(a). This approach features several advantages. ChGs are known for their infrared transparency, which is exceptionally broadband [35] and enables low-loss passive operation over the entire mid-IR spectral regime (2.5–20 μm). Their high refractive indices (2–3.5) also produce strong optical confinement and index matching to III-V semiconductors, for efficient coupling to active III-V components with low Fresnel reflection losses. And unlike most other amorphous films, ChGs can be deposited and processed near room temperature in a non-oxidizing ambient [36]. This minimizes damage and/or modification (e.g., due to diffusion) of the lasers and other semiconductor nanostructures to preserve high material quality without compromising device performance. Last but not least, ChG photonics provides a highly versatile integration platform on which components such as spectroscopic sensors, photodetectors, and high-Q ring resonators have been experimentally validated [37–41]. While the present work demonstrates on-chip coupling of ChGs to ICLs, similar schemes that integrate ChGs with QCLs, interband and quantum cascade detectors (ICDs and QCDs), and other active III-V components are envisioned.

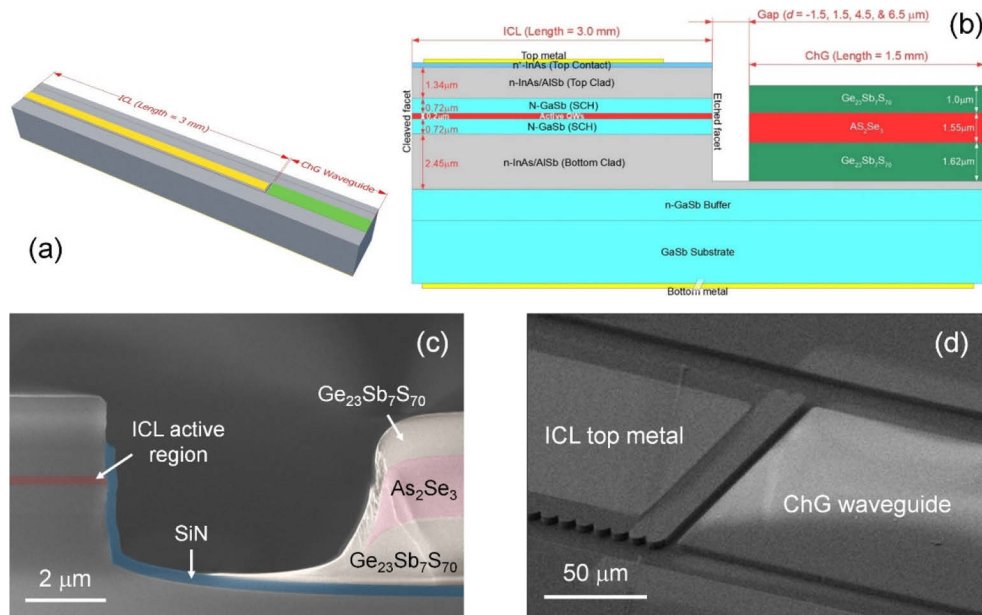


Fig. 1. (a) Schematic of an ICL (3 mm long) butt coupled to a ChG waveguide (1 or 1.5 mm long); (b) side-view cross-sectional schematic of the butt-coupled ICL and ChG waveguides separated by a gap of variable width (d); (c) cross-section and (d) tilted view SEM images of a ChG waveguide-integrated ICL device with $d = 6.5 \mu\text{m}$.

The ICL structure [27] (shown schematically in the left portion of Fig. 1(b)) comprises an n -GaSb (100) substrate and grown buffer layer, bottom InAs-AlSb superlattice (SL) optical cladding layer (2.4 μm), bottom n^- -GaSb separate confinement layer (SCL, 700 nm), 5 active gain stages, top SCL (700 nm), top SL clad layer (1.2 μm), and n^+ -InAs top contacting layer (20 nm). Thin transition superlattices separate the various regions to avoid abrupt discontinuities

of the conduction band offset. The structure was grown on a Riber Compact 21 T molecular beam epitaxy (MBE) system, using procedures similar to those reported previously [42]. Pulsed characterization of standard broad-area test devices with 150 μm ridge width, 2 mm cavity length, and uncoated facets indicated a threshold current density of 230 A/cm^2 , slope efficiency of 380 mW/A , and centroid wavelength of $\lambda = 3.24 \mu\text{m}$ at $T = 300 \text{ K}$.

Broad-area (150- μm wide) ICL ridges with corrugated sidewalls were fabricated by photolithography and BCl_3/Ar inductively coupled plasma (ICP) reactive ion etching (RIE), using procedures that have been described previously [43,44]. The etch proceeded through the active core to prevent lateral current spreading. In parallel with the RIE of the ridge sidewalls, a facet was etched at one end of the ridge for output to the ChG waveguide that would be deposited and patterned subsequently. Dielectric was then deposited on the sidewalls, and contact metallization on top of the ridge, terminating $\approx 20 \mu\text{m}$ short of the front and back facets. The chip was then cleaved to provide a mirror at the uncoated back facet of each 3-mm-long laser cavity.

A thick negative-tone resist mask was then defined, using contact lithography for lift-off patterning of the ChG waveguides. The mask provided a series of gap values between the ICL front facet and ChG waveguide, across which light from the ICL was coupled into the ChG. This was followed by sequential evaporation of the ChG layers, using a glass deposition process that was described in detail elsewhere [36]. The ChG waveguides with lengths 0.75-1.5 mm were patterned by sonication in an organic solvent bath to remove the resist mask. The ChG waveguide comprises an As_2Se_3 ($n = 2.78$) core sandwiched between $\text{Ge}_{23}\text{Sb}_7\text{S}_{70}$ ($n = 2.13$) top and bottom claddings, as shown schematically in the right portion of Fig. 1(b). This platform has yielded low propagation losses down to 0.7 dB/cm in the mid-IR [37]. The bottom cladding thickness was chosen to align the height of the As_2Se_3 ChG core layer with that of the ICL active stages, so as to facilitate butt coupling of the two waveguides. The schematic cross-section in Fig. 1(b) shows the layering in each waveguide, the relative heights, and the narrow air gap that separates them. Since the divergence of the ICL output beam along the vertical axis is approximately $\pm 26^\circ$ in air, the width of the air gap (d) between the two facets influences the fraction of light captured by the ChG waveguide. A series of gap widths were processed to determine the impact on coupling efficiency, as will be discussed further below.

Figure 1(c) and 1(d) show scanning electron microscopy (SEM) images of the processed waveguides in cross-sectional and tilted view, respectively, for a device with $d = 6.5 \mu\text{m}$. We see that the ChG waveguide end facet is slanted, which is typical of the lift-off patterning process [45]. However, this can be mitigated in future development, for instance, by using plasma etching to attain a vertical edge profile [46]. The SEM images indicate successful deposition of the CHG waveguides, although the air gaps are $\sim 1.5 \mu\text{m}$ wider than expected. This was most likely due to misalignment of the contact lithography. The resulting series of gap widths is $d = -1.5, 1.5, 4.5,$ and $6.5 \mu\text{m}$, where negative d indicates that the ChG deposition overlapped the top of the etched ICL end facet (so there was no air gap). The cleaved output facets of the CHG waveguides appear clean.

The processed chip was attached to a temperature-controlled C-mount and wire bonded for optical testing. Figure 2(a) shows a chip with three mounted lasers. To assess the optical and electrical performance, we measured the light-current-voltage (L - I - V) characteristics of the integrated lasers at 300 K, using free-space receiving optics with an $f/1$ lens and magnification ~ 14 to project the laser output to a photodetector. Imaging with an InSb focal plane array confirmed that light was collected only from the ChG waveguide, with negligible contributions, *e.g.*, of scattered light from the laser or emission from the substrate. For reference, we also measured the output from an ICL of identical size, but with two cleaved facets and no coupling to a ChG waveguide.

Figure 2(b) plots the I - V characteristics of four integrated ICLs with different gap widths d , along with the reference device that did not couple to a ChG waveguide. We see that while the

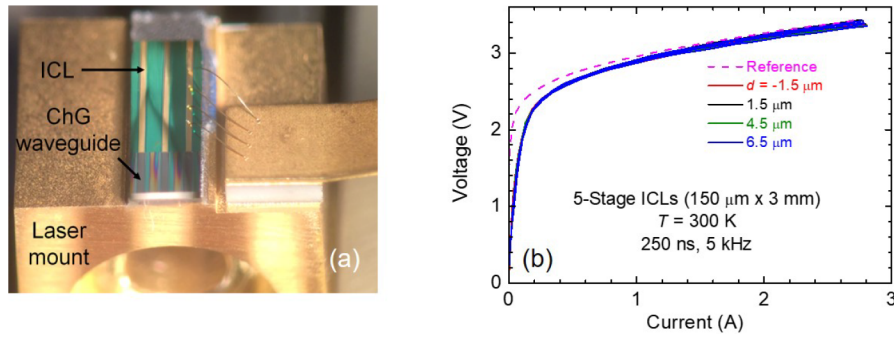


Fig. 2. (a) Microscope image of integrated devices on a C-mount; (b) I - V characteristics of the ChG waveguide-integrated ICLs with different gap widths, and the reference device.

curves for the integrated ICLs are quite consistent, their voltage turn-on is softer than for the reference laser. This indicates higher leakage current, most likely due to sidewall damage when the ridges were etched by BCl_3/Ar RIE to provide a vertical end facet. The reference ICL with two cleaved facets was processed by wet etching, which is known to induce minimal surface damage. In future work, the sidewall damage can be minimized by substituting a CH_4/Cl_2 -based dry etch [29].

Figure 3(a) shows L - I curves for up to five waveguide-integrated lasers with each gap value. While all the lasers exhibit quite similar threshold current densities of $\approx 280 \text{ A/cm}^2$, the devices with overlapping waveguides or smallest gap values (*i.e.*, $d = -1.5 \mu\text{m}$ and $1.5 \mu\text{m}$) display the highest slope efficiencies of up to 100 mW/A . The corresponding L - I curve for the reference ICL in Fig. 3(b) indicates a threshold current density of 190 A/cm^2 and slope efficiency of 260 mW/A . The lower threshold for the reference ICL is again attributable to leakage at the BCl_3 -etched sidewalls of the waveguide-integrated devices.

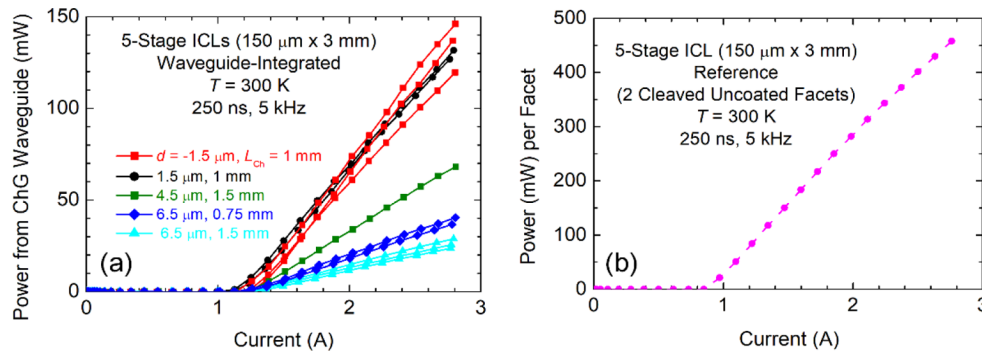


Fig. 3. L - I curves for the ChG waveguide-integrated ICLs (a) and the reference device (b).

We note here that if the ChG deposition forms a smooth optical interface when the air gap is negative (overlap of the two waveguides), the negative-gap structure should experience a slightly lower reflection at the laser cavity's output mirror than when an air gap is present (although feedback due to reflection across the gap by an external ChG surface will also affect the laser characteristics). This may account for the slightly higher thresholds for devices with $d = -1.5 \mu\text{m}$ vs. $+1.5 \mu\text{m}$, but also slightly higher slope efficiencies for two of the three ridges.

The ratio of each slope efficiency to that of the reference laser provides a first approximation to the efficiency of coupling between the III-V and ChG waveguides across the gap. The resulting

value represents a lower bound, however, because the loss in the ChG waveguide and sidewall leakage in the ICL also affect the slope efficiency of the integrated structure. The points in Fig. 4(a) plot this lower bound as a function of air gap width. We see that the coupling is strongest when the waveguides overlap ($d = -1.5 \mu\text{m}$) or the air gap is small ($1.5 \mu\text{m}$), whereas it decreases rapidly at larger gaps (4.5 and $6.5 \mu\text{m}$). The highest efficiency of $\geq 38\%$ represents a coupling loss ≤ -4.2 dB. The curve in Fig. 4(a) presents a simulation of the coupling efficiency that was obtained using the finite-difference time-domain (FDTD) method. The simulated and measured dependencies are in good agreement considering the non-ideal waveguide profiles, sidewall leakage, and other experimental uncertainties.

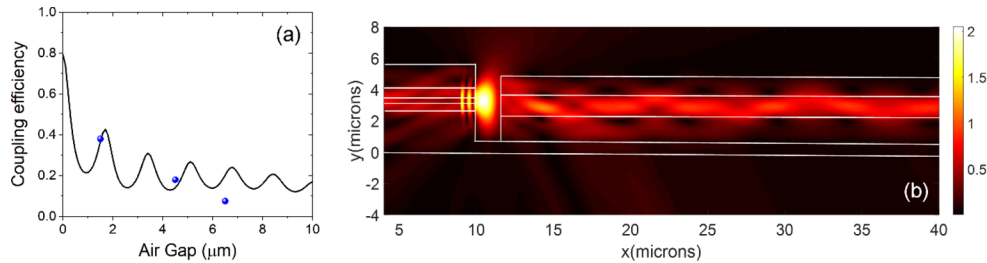


Fig. 4. (a) Simulated (curve) and measured (points) coupling efficiency from the ICL to the ChG waveguide as a function of air gap width, d , separating the two facets; (b) cross section of the simulated optical intensity profile for the case $d = 1.5 \mu\text{m}$.

To summarize, we experimentally demonstrated the monolithic integration of interband cascade lasers with passive photonic components made of chalcogenide glass. Peak powers up to 150 mW (with no roll-over) are observed, and the efficiencies for coupling light from the ICL to the low-loss ChG waveguide are $\geq 38\%$ when the air gap is small ($1.5 \mu\text{m}$) or the two waveguides overlap. This represents a lower bound because it neglects both sidewall leakage in the dry-etched integrated lasers and loss in the ChG waveguide following optical transfer. The observed coupling is considerably more efficient than has been observed to date between QCLs and ICLs integrated on silicon to passive silicon waveguides, via tapering of the III-V portion of the hybrid gain waveguide [47]. Our coupling efficiency is comparable to the theoretical value of 40% for transferring light from a QCL to a QCD that were both grown as part of the same vertical stack [48], and 42% determined from relative outputs following vertical coupling of a QCL to a passive III-V waveguide [49].

Several relatively straightforward improvements may further enhance the observed performance. For example, the lithography and alignment accuracy can be improved to minimize the air gap width for lower loss. In fact, the coupling appears to remain nearly optimal when the gap is eliminated altogether by overlapping the two waveguides, which will be far more tolerant to alignment inaccuracies. Or a narrow air gap can be filled with a high-index medium (*e.g.*, solution-derived ChGs [50]) to suppress beam expansion in the free-propagating region. In these initial experiments, a multi-mode ChG waveguide was employed to match the large mode size of the broad area ICL. However, our approach is equally adaptable to coupling between much narrower single-mode waveguides that will most likely provide the basis for functional photonic integrated circuits in the future.

We also show that due to the low processing temperatures of ChGs, the integration process does not adversely impact the laser performance. Since we have already demonstrated the patterning of multiple ICLs and ChG waveguides on the same chip as in Fig. 2(a), the scheme is clearly suitable for constructing PICs that combine multiple lasers with other active devices such as interband cascade detectors. The approach can also be expanded to more diverse substrate platforms that combine III-Vs and SiGeSn. For example, the large Kerr nonlinearity of ChGs [51] makes them

suitable candidates for mid-IR supercontinuum [17] or frequency comb generation [52]. Our work opens the door to fully integrated ICL- or QCL-pumped on-chip nonlinear sources, which may find broad applications in spectroscopic sensing and free-space communications.

Funding. Office of Naval Research; National Science Foundation (1200406).

Acknowledgments. This work was funded by NSF under award number 1200406. NRL was funded by the Office of Naval Research.

Disclosures. The authors declare that there are no conflicts of interest related to this article.

Data availability. Data underlying the results presented in this paper are not publicly available at this time but may be obtained from the authors upon reasonable request.

References

1. P. T. Lin, V. Singh, J. F. Wang, H. T. Lin, J. J. Hu, K. Richardson, J. D. Musgraves, I. Luzinov, J. Hensley, L. C. Kimerling, and A. Agarwal, "Si-CMOS compatible materials and devices for mid-IR microphotonic," *Opt. Mater. Express* **3**(9), 1474–1487 (2013).
2. G. Roelkens, U. Dave, A. Gassenq, N. Hattasan, C. Hu, B. Kuyken, F. Leo, A. Malik, M. Muneeb, E. Ryckeboer, S. Uvin, Z. Hens, R. Baets, Y. Shimura, F. Gencarelli, B. Vincent, R. Loo, J. Van Campenhout, L. Cerutti, J. B. Rodriguez, E. Tournie, X. Chen, M. Nedeljkovic, G. Mashanovich, L. Shen, N. Healy, A. C. Peacock, X. P. Liu, R. Osgood, and W. Green, "Silicon-based heterogeneous photonic integrated circuits for the mid-infrared," *Opt. Mater. Express* **3**(9), 1523–1536 (2013).
3. H. Lin, Z. Luo, T. Gu, L. C. Kimerling, K. Wada, A. Agarwal, and J. Hu, "Mid-infrared integrated photonics on silicon: a perspective," *Nanophotonics* **7**(2), 393–420 (2017).
4. J. M. Fedeli and S. Nicoletti, "Mid-infrared (Mid-IR) silicon-based photonics," *Proc. IEEE* **106**(12), 2302–2312 (2018).
5. Y. Zou, S. Chakravarty, C. J. Chung, X. C. Xu, and R. T. Chen, "Mid-infrared silicon photonic waveguides and devices Invited," *Photonics Res.* **6**(4), 254–276 (2018).
6. J. R. Meyer, C. S. Kim, M. Kim, C. L. Canedy, C. D. Merritt, W. W. Bewley, and I. Vurgaftman, "Interband cascade photonic integrated circuits on native III-V chip," *Sensors* **21**(2), 599 (2021).
7. Y. Chen, H. T. Lin, J. J. Hu, and M. Li, "Heterogeneously integrated silicon photonics for the mid-infrared and spectroscopic sensing," *ACS Nano* **8**(7), 6955–6961 (2014).
8. J. Midkiff, K. M. Yoo, J. D. Shin, H. Dalir, M. Teimourpour, and R. T. Chen, "Optical phased array beam steering in the mid-infrared on an InP-based platform," *Optica* **7**(11), 1544–1547 (2020).
9. Y. L. Su, W. Wang, X. H. Hu, H. Hu, X. N. Huang, Y. S. Wang, J. H. Si, X. P. Xie, B. Han, H. Feng, Q. Hao, G. S. Zhu, T. Duan, and W. Zhao, "10 Gbps DPSK transmission over free-space link in the mid-infrared," *Opt. Express* **26**(26), 34515–34528 (2018).
10. Z. Han, P. Lin, V. Singh, L. Kimerling, J. Hu, K. Richardson, A. Agarwal, and D. T. H. Tan, "On-chip mid-infrared gas detection using chalcogenide glass waveguide," *Appl. Phys. Lett.* **108**(14), 141106 (2016).
11. M. J. Yu, Y. Okawachi, A. G. Griffith, N. Picque, M. Lipson, and A. L. Gaeta, "Silicon-chip-based mid-infrared dual-comb spectroscopy," *Nat. Commun.* **9**(1), 1869 (2018).
12. S. A. Miller, M. J. Yu, X. C. Ji, A. G. Griffith, J. Cardenas, A. L. Gaeta, and M. Lipson, "Low-loss silicon platform for broadband mid-infrared photonics," *Optica* **4**(7), 707–712 (2017).
13. R. Shankar, R. Leijssen, I. Bulu, and M. Loncar, "Mid-infrared photonic crystal cavities in silicon," *Opt. Express* **19**(6), 5579–5586 (2011).
14. S. Deckoff-Jones, H. T. Lin, D. Kita, H. Y. Zheng, D. H. Li, W. Zhang, and J. J. Hu, "Chalcogenide glass waveguide-integrated black phosphorus mid-infrared photodetectors," *J. Opt.* **20**(4), 044004 (2018).
15. M. Montesinos-Ballester, V. Vakarin, J. M. Ramirez, Q. Liu, C. Alonso-Ramos, X. Le Roux, J. Frigerio, A. Ballabio, A. Barzaghi, L. Deniel, D. Bouville, L. Vivien, G. Isella, and D. Marris-Morini, "Optical modulation in Ge-rich SiGe waveguides in the mid-infrared wavelength range up to 11 μm ," *Commun. Mater.* **1**(1), 6 (2020).
16. J. Chiles and S. Fathpour, "Mid-infrared integrated waveguide modulators based on silicon-on-lithium-niobate photonics," *Optica* **1**(5), 350–355 (2014).
17. Q. Y. Du, Z. Q. Luo, H. K. Zhong, Y. F. Zhang, Y. Z. Huang, T. J. Du, W. Zhang, T. Gu, and J. J. Hu, "Chip-scale broadband spectroscopic chemical sensing using an integrated supercontinuum source in a chalcogenide glass waveguide," *Photonics Res.* **6**(6), 506–510 (2018).
18. Z. Li, Q. Y. Du, C. P. Wang, J. H. Zou, T. J. Du, K. A. Richardson, Z. P. Cai, J. J. Hu, and Z. Q. Luo, "Externally pumped photonic chip-based ultrafast Raman soliton source," *Laser Photonics Rev.* **15**(2), 2000301 (2021).
19. Y. Y. Zhou, Y. H. Miao, S. Ojo, H. Tran, G. Abernathy, J. M. Grant, S. Amoah, G. Salamo, W. Du, J. F. Liu, J. Margetis, J. Tolle, Y. H. Zhang, G. Sun, R. A. Soref, B. H. Li, and S. Q. Yu, "Electrically injected GeSn lasers on Si operating up to 100 K," *Optica* **7**(8), 924–928 (2020).
20. S. Wirths, R. Geiger, N. von den Driesch, G. Mussler, T. Stoica, S. Mantl, Z. Ikonik, M. Luysberg, S. Chiussi, J. M. Hartmann, H. Sigg, J. Faist, D. Buca, and D. Grutzmacher, "Lasing in direct-bandgap GeSn alloy grown on Si," *Nat. Photonics* **9**(2), 88–92 (2015).

21. M. R. Calvo, L. M. Bartolome, M. Bahriz, G. Boissier, L. Cerutti, J. B. Rodriguez, and E. Tournie, "Mid-infrared laser diodes epitaxially grown on on-axis (001) silicon," *Optica* **7**(4), 263–266 (2020).
22. A. Spott, J. Peters, M. L. Davenport, E. J. Stanton, C. D. Merritt, W. W. Bewley, I. Vurgaftman, C. S. Kim, J. R. Meyer, J. Kirch, L. J. Mawst, D. Botez, and J. E. Bowers, "Quantum cascade laser on silicon," *Optica* **3**(5), 545–551 (2016).
23. A. Spott, E. J. Stanton, A. Torres, M. L. Davenport, C. L. Canedy, I. Vurgaftman, M. J. Kim, C. S. Kim, C. D. Merritt, W. W. Bewley, J. R. Meyer, and J. E. Bowers, "Interband cascade laser on silicon," *Optica* **5**(8), 996–1005 (2018).
24. J. Faist, F. Capasso, D. L. Sivco, C. Sirtori, A. L. Hutchinson, and A. Y. Cho, "Quantum cascade laser," *Science* (New York, N.Y.) **264**(5158), 553–556 (1994).
25. J. Faist, *Quantum Cascade Lasers* (OUP Oxford, 2013).
26. R. Q. Yang, "Infrared laser based on intersubband transitions in quantum wells," *Superlattices Microstruct.* **17**(1), 77–83 (1995).
27. J. R. Meyer, W. W. Bewley, C. L. Canedy, C. S. Kim, M. Kim, C. D. Merritt, and I. Vurgaftman, "The interband cascade laser," *Photonics* **7**(3), 75 (2020).
28. J. R. Meyer, I. Vurgaftman, R. Q. Yang, and L. R. Ram-Mohan, "Type-II and type-I interband cascade lasers," *Electron. Lett.* **32**(1), 45 (1996).
29. I. Vurgaftman, R. Weih, M. Kamp, J. R. Meyer, C. L. Canedy, C. S. Kim, M. Kim, W. W. Bewley, C. D. Merritt, J. Abell, and S. Höfling, "Interband cascade lasers," *J. Phys. D: Appl. Phys.* **48**(12), 123001 (2015).
30. H. Lotfi, L. Li, S. M. S. Rassel, R. Q. Yang, C. J. Correge, M. B. Johnson, P. R. Larson, and J. A. Gupta, "Monolithically integrated mid-IR interband cascade laser and photodetector operating at room temperature," *Appl. Phys. Lett.* **109**(15), 151111 (2016).
31. B. Schwarz, C. A. Wang, L. Missaggia, T. S. Mansuripur, P. Chevalier, M. K. Connors, D. McNulty, J. Cederberg, G. Strasser, and F. Capasso, "Watt-level continuous-wave emission from a bifunctional quantum cascade laser/detector," *ACS Photonics* **4**(5), 1225–1231 (2017).
32. J. Montoya, C. Wang, A. Goyal, K. Creedon, M. Connors, J. Daulton, J. Donnelly, L. Missaggia, C. Aleshire, A. Sanchez-Rubio, and W. Herzog, "Integration of quantum cascade lasers and passive waveguides," *Appl. Phys. Lett.* **107**(3), 031110 (2015).
33. S. Chakravarty, J. Midkiff, K. Yoo, A. Rostamian, and R. Chen, *Monolithic Integration of Quantum Cascade Laser, Quantum Cascade Detector, and Subwavelength Waveguides for Mid-infrared Integrated Gas Sensing* (SPIE, 2019).
34. C. Tsay, F. Toor, C. F. Gmachl, and C. B. Arnold, "Chalcogenide glass waveguides integrated with quantum cascade lasers for on-chip mid-IR photonic circuits," *Opt. Lett.* **35**(20), 3324–3326 (2010).
35. B. J. Eggleton, B. Luther-Davies, and K. Richardson, "Chalcogenide photonics," *Nat. Photonics* **5**(3), 141–148 (2011).
36. L. Li, H. Lin, S. Qiao, Y. Zou, S. Danto, K. Richardson, J. D. Musgraves, N. Lu, and J. Hu, "Integrated flexible chalcogenide glass photonic devices," *Nat. Photonics* **8**(8), 643–649 (2014).
37. H. T. Lin, L. Li, Y. Zou, S. Danto, J. D. Musgraves, K. Richardson, S. Kozacik, M. Murakowski, D. Prather, P. T. Lin, V. Singh, A. Agarwal, L. C. Kimerling, and J. J. Hu, "Demonstration of high-Q mid-infrared chalcogenide glass-on-silicon resonators," *Opt. Lett.* **38**(9), 1470–1472 (2013).
38. V. Singh, P. T. Lin, N. Patel, H. T. Lin, L. Li, Y. Zou, F. Deng, C. Y. Ni, J. J. Hu, J. Giammarco, A. P. Soliani, B. Zdyrko, I. Luzinov, S. Novak, J. Novak, P. Wachtel, S. Danto, J. D. Musgraves, K. Richardson, L. C. Kimerling, and A. M. Agarwal, "Mid-infrared materials and devices on a Si platform for optical sensing," *Sci. Technol. Adv. Mater.* **15**(1), 014603 (2014).
39. P. Ma, D. Y. Choi, Y. Yu, Z. Y. Yang, K. Vu, T. Nguyen, A. Mitchell, B. Luther-Davies, and S. Madden, "High Q factor chalcogenide ring resonators for cavity-enhanced MIR spectroscopic sensing," *Opt. Express* **23**(15), 19969–19979 (2015).
40. Z. Han, V. Singh, D. Kita, C. Monmeyran, P. Becla, P. Su, J. Li, X. Huang, L. C. Kimerling, J. Hu, K. Richardson, D. T. H. Tan, and A. Agarwal, "On-chip chalcogenide glass waveguide-integrated mid-infrared PbTe detectors," *Appl. Phys. Lett.* **109**(7), 071111 (2016).
41. P. Su, Z. Han, D. Kita, P. Becla, H. Lin, S. Deckoff-Jones, K. Richardson, L. C. Kimerling, J. Hu, and A. Agarwal, "Monolithic on-chip mid-IR methane gas sensor with waveguide-integrated detector," *Appl. Phys. Lett.* **114**(5), 051103 (2019).
42. C. L. Canedy, C. S. Kim, M. Kim, D. C. Larrabee, J. A. Nolde, W. W. Bewley, I. Vurgaftman, and J. R. Meyer, "High-power, narrow-ridge, mid-infrared interband cascade lasers," *J. Vac. Sci. Technol., B: Microelectron. Nanometer Struct.–Process., Meas., Phenom.* **26**(3), 1160–1162 (2008).
43. I. Vurgaftman, C. L. Canedy, C. S. Kim, M. Kim, W. W. Bewley, J. R. Lindle, J. Abell, and J. R. Meyer, "Mid-infrared interband cascade lasers operating at ambient temperatures," *New J. Phys.* **11**(12), 125015 (2009).
44. M. Kim, C. Kim, W. Bewley, C. Merritt, C. Canedy, J. Abell, I. Vurgaftman, and J. Meyer, *Interband Cascade Lasers with High CW Power and Brightness* (SPIE, 2015).
45. J. J. Hu, V. Tarasov, N. Carlie, N. N. Feng, L. Petit, A. Agarwal, K. Richardson, and L. Kimerling, "Si-CMOS-compatible lift-off fabrication of low-loss planar chalcogenide waveguides," *Opt. Express* **15**(19), 11798–11807 (2007).
46. Q. Y. Du, Y. Z. Huang, J. Y. Li, D. Kita, J. Michon, H. T. Lin, L. Li, S. Novak, K. Richardson, W. Zhang, and J. J. Hu, "Low-loss photonic device in Ge-Sb-S chalcogenide glass," *Opt. Lett.* **41**(13), 3090–3093 (2016).

47. A. Malik, A. Spott, E. J. Stanton, J. D. Peters, J. D. Kirch, L. J. Mawste, D. Botez, J. R. Meyer, and J. E. Bowers, "Integration of mid-infrared light sources on silicon-based waveguide platforms in 3.5–4.7 μm wavelength range," *IEEE J. Sel. Top. Quantum Electron.* **25**(6), 1–9 (2019).
48. M. Hitaka, T. Dougakiuchi, A. Ito, K. Fujita, and T. Edamura, "Stacked quantum cascade laser and detector structure for a monolithic mid-infrared sensing device," *Appl. Phys. Lett.* **115**(16), 161102 (2019).
49. S. Jung, D. Palaferri, K. Zhang, F. Xie, Y. Okuno, C. Pinzone, K. Lascola, and M. A. Belkin, "Homogeneous photonic integration of mid-infrared quantum cascade lasers with low-loss passive waveguides on an InP platform," *Optica* **6**(8), 1023–1030 (2019).
50. Y. L. Zha, M. Waldmann, and C. B. Arnold, "A review on solution processing of chalcogenide glasses for optical components," *Opt. Mater. Express* **3**(9), 1259–1272 (2013).
51. J. G. Zhu, M. Zohrabi, K. Bae, T. M. Horning, M. B. Grayson, W. Park, and J. T. Gopinath, "Nonlinear characterization of silica and chalcogenide microresonators," *Optica* **6**(6), 716–722 (2019).
52. D. Xia, Z. Yang, P. Zeng, Y. Huang, Y. Sun, J. Pan, J. Song, Y. Zhu, H. Guo, B. Zhang, and Z. Li, "Integrated Ge-Sb-S chalcogenide microresonator on chip for nonlinear photonics," in *14th Pacific Rim Conference on Lasers and Electro-Optics (CLEO PR 2020)* (Optical Society of America, Sydney, 2020), p. C3C_1.